Research Square

Preprints are preliminary reports that have not undergone peer review.
They should not be considered conclusive, used to inform clinical practice,
or referenced by the media as validated information.

Excitonic nonlinear optical response of conventional and inverted CdSe/ZnS cylindrical core/shell quantum dots under dual-interface dielectric confinement: saturable absorption, photobleaching, and dielectric engineering

Lakhdar Sek

lakhdar-sek@univ-eloued.dz

University of Eloued

Research Article

Keywords: CdSe/ZnS quantum dots, cylindrical core/shell nanostructures, exciton binding energy, dual-interface dielectric confinement, saturable absorption, nonlinear optical absorption, refractive-index change, photobleaching, image-charge effects, local-field correction, temperature-dependent dephasing, optical limiter, all-optical switching

Posted Date: June 29th, 2026

DOI: https://doi.org/10.21203/rs.3.rs-10020954/v1

License: This work is licensed under a Creative Commons Attribution 4.0 International License.
Read Full License

Additional Declarations: No competing interests reported.

Excitonic nonlinear optical response of conventional and inverted CdSe/ZnS cylindrical core/shell quantum dots under dual-interface dielectric confinement: saturable absorption, photobleaching, and dielectric engineering

Sek Lakhdar[1*]

[1*]NTDL Laboratory, Faculty of Technology, University of El Oued, El Oued, 39000, Algeria.

Corresponding author(s). E-mail(s): lakhdar-sek@univ-eloued.dz;

Abstract

Inverting the core/shell geometry of a CdSe/ZnS cylindrical quantum dot — placing the optically active CdSe layer in the shell rather than the core — relocates the exciton from the nanostructure centre to a ring-like shell state and amplifies the peak third-order nonlinear absorption coefficient by up to 5.1 % relative to the conventional geometry, an enhancement that is invisible to single-particle models and grows monotonically with the matrix permittivity. To establish this result rigorously, we develop an excitonic theoretical framework that simultaneously incorporates four physical ingredients absent from previous treatments of oxide-embedded cylindrical core/shell quantum dots (CSQDs): (i) electron–hole Coulomb correlation via a variational product ansatz, yielding a binding-energy redshift of $\boldsymbol{E_b} \approx \mathbf{80}$–140 meV that single-particle models systematically miss; (ii) dual-interface dielectric self-polarisation accounting for image-charge effects at both the internal CdSe/ZnS boundary and the external shell/matrix boundary, with cross-coupling that adds up to 18 meV (roughly 8 % of the room-temperature linewidth) compared with single-interface approximations; (iii) matrix-dependent local-field correction within the Clausius–Mossotti approximation; and (iv) temperature-dependent excitonic dephasing via the probability-weighted Rudin–Reinecke–Segall model, which raises the photobleaching threshold by a factor of $\approx \mathbf{345}$ between 50 K and 400 K through the scaling $\boldsymbol{I_c \propto \gamma_\lambda^2/|M_{0\lambda}|^2}$. Linear and third-order nonlinear optical responses

are computed using density-matrix formalism. The inverted ZnS/CdSe geometry (ICCSQD) in HfO_2 achieves a linear absorption exceeding $4 \times 10^5\ m^{-1}$, the largest oscillator strength among all four CCSQD/ICCSQD × SiO_2/HfO_2 configurations, and nonlinear absorption and refractive-index change enhancements of 5.098 % and 0.997 % relative to the conventional geometry. An analytical scaling argument demonstrates that the absorptive nonlinearity is more dielectrically tunable than the dispersive one because a $1/E_{fi}^{exc}$ factor in the dispersive channel partially cancels the local-field enhancement, suppressing the permittivity dependence of $\eta_{\Delta n}$. These results provide quantitative, physically transparent design guidelines for oxide-embedded quantum-dot saturable absorbers, optical limiters, and all-optical switching devices.

Keywords: CdSe/ZnS quantum dots, cylindrical core/shell nanostructures, exciton binding energy, dual-interface dielectric confinement, saturable absorption, nonlinear optical absorption, refractive-index change, photobleaching, image-charge effects, local-field correction, temperature-dependent dephasing, optical limiter, all-optical switching

1 Introduction

Core/shell quantum dots (CSQDs) composed of II–VI, IV–VI or III–V semiconductor materials have emerged as versatile building blocks for advanced optoelectronic, photonic and sensing technologies [1–3]. Among the many material combinations, CdSe/ZnS has become one of the most extensively studied type-I systems owing to its high photoluminescence quantum yield, efficient surface passivation by the ZnS shell, improved chemical stability, and broad spectral tunability across the visible range [4–6]. These properties have enabled CdSe/ZnS quantum dots to be exploited in light-emitting diodes [7, 8], biological imaging [9, 10], colour-conversion displays [11], and nonlinear optical devices [12, 13].

Depending on the synthesis route, CSQDs can adopt spherical, cylindrical, ellipsoidal, pyramidal and conical shapes [14, 15]. Cylindrical geometries offer an important practical advantage: quantum confinement can be tuned independently through the radius and the height, providing greater structural freedom than spherical dots, where a single radius controls the confinement [16–18].

In addition to the standard CdSe-core/ZnS-shell configuration, the inverted ZnS-core/CdSe-shell geometry has recently attracted attention because the optically active CdSe region is shifted from the centre of the nanostructure to the shell, strongly modifying the spatial distribution of the confined carriers and enhancing their interaction with the surrounding dielectric environment [16, 19, 20]. Naifar and Hasanirokh [16] showed that inverted ZnS/CdSe cylindrical CSQDs embedded in oxide matrices can exhibit stronger optical absorption and refractive-index changes than conventional CdSe/ZnS structures. However, their treatment rests on a single-electron effective-mass model that omits the hole, electron–hole Coulomb attraction, exciton binding energy, and temperature-dependent excitonic dephasing — all of which are essential for an accurate description of optical spectra in CdSe-based nanostructures [21–23].

The role of the surrounding dielectric environment is particularly important in realistic devices because nanocrystals are rarely isolated; they are embedded in polymers, oxides, glasses, solvents or multilayer stacks. Experimental studies have shown that the host medium can significantly modify absorption and emission wavelengths [24–26], quantum yields [27], and charge-storage performance [28]. Theoretically, dielectric matrices have been shown to alter optical susceptibilities in II–VI quantum dots [29–32], third-harmonic generation in silicon quantum dots [33], and the complex dielectric response of CdS/ZnS cylindrical systems [17]. Among oxide matrices, SiO_2 ($\varepsilon_m = 3.9$) and HfO_2 ($\varepsilon_m = 25$) represent two important limiting cases: SiO_2 is a low-permittivity oxide with excellent transparency and chemical stability, whereas HfO_2 is a high-permittivity oxide widely used in CMOS-compatible and quantum-dot memory architectures [28, 34–36]. Comparing these two matrices provides a direct window into the transition from weak to strong dielectric screening, spanning nearly a factor of six in permittivity.

Despite significant progress in modelling oxide-embedded CSQDs, three important physical limitations persist in the literature. *First*, many theoretical treatments rely on single-particle models [16, 17, 37–40] in which the hole and the electron–hole Coulomb interaction are neglected. This approximation is inadequate for CdSe-based quantum dots, whose optical spectra are fundamentally excitonic in nature [21–23]. Since the bulk exciton Bohr radius of CdSe is $a_B^* \approx 5.6\,\mathrm{nm}$, comparable to the dimensions of cylindrical CSQDs studied here, excitonic correlation produces a binding-energy redshift of 80–140 meV (Section 3.3) that directly shifts the operating wavelength by 30–60 nm — an error large enough to invalidate device-design calculations that rely on a specific operating wavelength. *Second*, the dielectric self-polarisation correction is commonly applied only at the outer shell/matrix boundary, using an averaged internal dielectric constant $\varepsilon_{\mathrm{in}} = \sqrt{\varepsilon_c \varepsilon_s}$ for the whole core/shell system [16, 17, 37]. This single-interface approximation neglects the coupling between image charges induced at the two interfaces, which contributes up to 18 meV in thin-shell geometries [41, 42] — roughly 8 % of the room-temperature homogeneous linewidth, and hence non-negligible for accurate line-shape prediction. *Third*, a temperature-independent phenomenological dephasing time $\tau = 300\,\mathrm{fs}$ [16, 17] is routinely assumed, whereas the excitonic linewidth in II–VI quantum dots depends strongly on temperature through acoustic-phonon scattering at low temperature and LO-phonon-assisted dephasing at higher temperature [43, 44]. Since the photobleaching threshold scales as $I_c \propto \gamma_\lambda^2/|M_{0\lambda}|^2$, temperature-dependent dephasing directly controls the nonlinear saturation behaviour and determines the practical operating range of a device.

The present work addresses all three limitations simultaneously. We show that inverting the core/shell geometry relocates the exciton from the nanostructure centre to a ring-like shell state adjacent to the oxide matrix, and that this relocation amplifies the peak third-order nonlinear absorption by up to 5.1 % relative to the conventional geometry through a combination of enhanced local-field coupling and stronger image-charge interaction with the high-permittivity matrix. This enhancement is invisible to single-particle models, which overestimate transition energies by 80–140 meV and therefore mispredict the detuning-dependent nonlinear coefficients. The novelty of this study is fourfold:

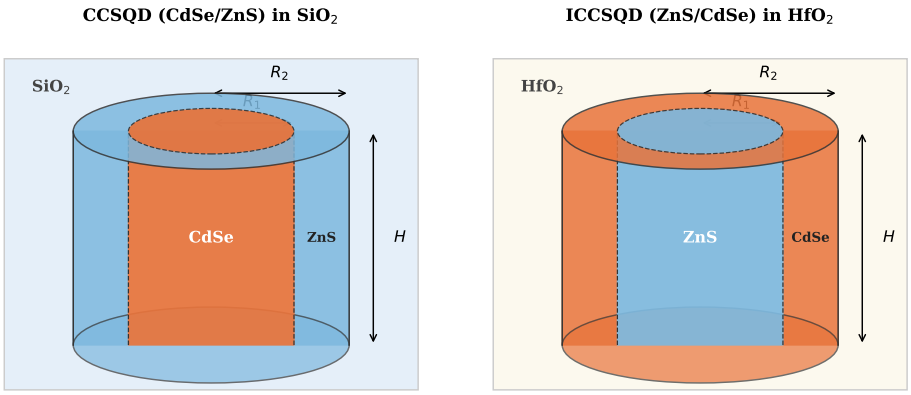


Fig. 1 Schematic illustration of the cylindrical core/shell quantum-dot geometries. **Left**: conventional CdSe/ZnS configuration (CCSQD) embedded in SiO_2. **Right**: inverted ZnS/CdSe configuration (ICCSQD) embedded in HfO_2. The core radius R_1, outer radius R_2, and height H are indicated. In the ICCSQD the active CdSe region lies adjacent to the oxide matrix, maximising sensitivity to the dielectric environment.

1. The optical transition is treated as a fully excitonic process involving both electron and hole confinement, and the exciton binding energy is evaluated explicitly and compared directly with the single-particle limit (Table 4).
2. A dual-interface dielectric self-polarisation model accounts for image-charge effects at *both* boundaries including their cross-coupling via a convergent multipole series; series convergence is verified in Section 2.3.2.
3. Temperature-dependent excitonic linewidth broadening is included through the probability-weighted Rudin–Reinecke–Segall model, and the photobleaching threshold $I_c(T)$ is computed quantitatively over 50–400 K (Section 3.8).
4. A physically transparent analytical scaling argument (Section 3.10) explains *why* the absorptive third-order nonlinearity is more dielectrically tunable than the dispersive one, and predicts the permittivity dependence of η_{NL} from first principles.

Section 2 presents the theoretical framework. Section 3 presents and discusses the numerical results. Section 4 summarises the conclusions and their device-design implications.

2 Theoretical Framework

2.1 Geometry and Material Configuration

We consider two cylindrical core/shell quantum-dot configurations embedded in an oxide dielectric matrix (Fig. 1). The *conventional cylindrical core/shell quantum dot* (CCSQD) consists of a CdSe core of radius R_1 surrounded by a concentric ZnS shell extending to outer radius R_2. The *inverted cylindrical core/shell quantum dot* (ICCSQD) reverses the material arrangement, placing ZnS in the core and CdSe in the shell. Both structures share height H along the z-axis and are embedded in SiO_2 ($\varepsilon_m = 3.9$) or HfO_2 ($\varepsilon_m = 25$) [34, 45].

The system is described in cylindrical coordinates $\mathbf{r} = (\rho, \varphi, z)$. The quantum-dot domain is

$$\Omega_{\mathrm{QD}} = \left\{(\rho, \varphi, z) : 0 \le \rho \le R_2,\ 0 \le \varphi < 2\pi,\ -\tfrac{H}{2} \le z \le \tfrac{H}{2}\right\}, \tag{1}$$

with core sub-domain $\Omega_c = \{0 \le \rho \le R_1\}$ and shell sub-domain $\Omega_s = \{R_1 < \rho \le R_2\}$. The material assignment is summarised in Table 1; the physical parameters are compiled in Table 2.

Table 1 Material configuration for the two quantum-dot architectures.

Region	CCSQD	ICCSQD
Core ($\rho \le R_1$)	CdSe	ZnS
Shell ($R_1 < \rho \le R_2$)	ZnS	CdSe
Matrix ($\rho > R_2$)	SiO_2 or HfO_2	

Table 2 Physical parameters used in the calculations. m_0 denotes the free-electron mass.

Parameter	Symbol	CdSe	ZnS	Ref.
Electron eff. mass	m_e^*/m_0	0.13	0.28	[46, 47]
Hole eff. mass	m_h^*/m_0	0.45	0.61	[46, 47]
Static dielectric const.	ε_r	10.6	8.9	[47, 48]
Band gap	E_g (eV)	1.74	3.68	[4, 47]
Bulk exciton Bohr radius	a_B^* (nm)	5.6	2.5	[21, 48]
Bulk exciton binding	E_b^{bulk} (meV)	15	40	[22, 48]
LO phonon energy	$\hbar\omega_{\mathrm{LO}}$ (meV)	26.0	43.9	[47, 49]
CB offset (ZnS/CdSe)	ΔE_c (eV)	0.90		[4]
VB offset (ZnS/CdSe)	ΔE_v (eV)	0.30		[4]
QD volume density	N_{QD} (m^{-3})	5.0×10^{24}		[16]
SiO_2 permittivity	ε_m	3.9		[34]
HfO_2 permittivity	ε_m	25.0		[34]

2.2 Single-Particle Hamiltonians and Boundary Conditions

Within the position-dependent effective-mass approximation, the single-particle Hamiltonian for carrier $a = e, h$ is [50, 51]

$$\hat{h}_a(\mathbf{r}) = -\nabla \cdot \left[\frac{\hbar^2}{2m_a^*(\mathbf{r})}\nabla\right] + V_a(\mathbf{r}) + \Sigma_a(\mathbf{r}). \tag{2}$$

The BenDaniel–Duke kinetic-energy operator ensures Hermiticity and probability-current conservation across effective-mass discontinuities [50]. The confinement potentials are:

CCSQD (CdSe core / ZnS shell):

$$V_e^{\mathrm{CCSQD}} = \begin{cases} 0, & \mathbf{r} \in \Omega_{\mathrm{CdSe}} \\ \Delta E_c, & \mathbf{r} \in \Omega_{\mathrm{ZnS}} \\ \infty, & \mathbf{r} \in \Omega_m \end{cases}, \quad V_h^{\mathrm{CCSQD}} = \begin{cases} 0, & \mathbf{r} \in \Omega_{\mathrm{CdSe}} \\ \Delta E_v, & \mathbf{r} \in \Omega_{\mathrm{ZnS}} \\ \infty, & \mathbf{r} \in \Omega_m \end{cases}. \tag{3}$$

ICCSQD (ZnS core / CdSe shell):

$$V_e^{\mathrm{ICCSQD}} = \begin{cases} \Delta E_c, & \mathbf{r} \in \Omega_{\mathrm{ZnS}} \\ 0, & \mathbf{r} \in \Omega_{\mathrm{CdSe}} \\ \infty, & \mathbf{r} \in \Omega_m \end{cases}, \quad V_h^{\mathrm{ICCSQD}} = \begin{cases} \Delta E_v, & \mathbf{r} \in \Omega_{\mathrm{ZnS}} \\ 0, & \mathbf{r} \in \Omega_{\mathrm{CdSe}} \\ \infty, & \mathbf{r} \in \Omega_m \end{cases}. \tag{4}$$

The infinite-barrier approximation at $\rho = R_2$ is justified by the large band gaps of the oxide matrices (SiO_2: $E_g \approx 9.0\,\mathrm{eV}$; HfO_2: $E_g \approx 5.7\,\mathrm{eV}$) relative to ZnS ($E_g \approx 3.68\,\mathrm{eV}$) [34, 52].

2.2.1 Separation of variables and radial equation

By cylindrical symmetry the envelope wavefunction separates as

$$\psi_{a,nm}(\rho, \varphi, z) = \frac{1}{\sqrt{2\pi}} R_{a,nm}(\rho)\, Z_n(z)\, e^{im\varphi}, \quad m = 0, \pm 1, \pm 2, \ldots, \tag{5}$$

where $Z_n(z) = \sqrt{2/H}\sin(n\pi z/H)$ contributes the axial kinetic energy $E_n^z = \hbar^2(n\pi/H)^2/(2m_a^*)$. The radial function satisfies Bessel's equation in each sub-domain j:

$$\frac{d^2 R_{a,nm}^{(j)}}{d\rho^2} + \frac{1}{\rho}\frac{dR_{a,nm}^{(j)}}{d\rho} + \left(\kappa_{a,j}^2 - \frac{m^2}{\rho^2}\right) R_{a,nm}^{(j)} = 0, \tag{6}$$

with $\kappa_{a,j}^2 = 2m_{a,j}^*/\hbar^2\big[E_{a,\nu} - V_{a,j} - \Sigma_a\big] - (n\pi/H)^2$. For $\kappa_{a,j}^2 > 0$ the solutions are ordinary Bessel functions J_m, Y_m; for $\kappa_{a,j}^2 < 0$ they are modified Bessel functions I_m, K_m. Regularity at $\rho = 0$ and the hard-wall condition at $\rho = R_2$ fix the integration constants.

2.2.2 BenDaniel–Duke interface conditions

At $\rho = R_1$ the BenDaniel–Duke conditions [50, 51] enforce:

$$R_{a,nm}^{-}\big|_{R_1} = R_{a,nm}^{+}\big|_{R_1}, \qquad \frac{1}{m_a^{*-}}\frac{dR_{a,nm}^{-}}{d\rho}\bigg|_{R_1} = \frac{1}{m_a^{*+}}\frac{dR_{a,nm}^{+}}{d\rho}\bigg|_{R_1}. \tag{7}$$

Together with $R_{a,nm}(R_2) = 0$, Eq. (7) yields a transcendental dispersion relation from which the discrete eigenvalues $E_{a,\nu}$ are extracted numerically.

2.3 Full Dual-Interface Dielectric Confinement

The CdSe/ZnS/matrix heterostructure contains *two* dielectric interfaces: Interface I at $\rho = R_1$ ($\varepsilon_c = 10.6$ vs $\varepsilon_s = 8.9$) and Interface II at $\rho = R_2$ (ε_s vs ε_m). Previous models applied a self-polarisation correction only at Interface II [16, 17, 37]. The present work employs a dual-interface Green-function treatment [41, 42, 53, 54] accounting for both boundaries and their coupling.

The self-polarisation energy $\Sigma_a = q_a^2 G_{\rm pol}(\mathbf{r}, \mathbf{r})/2$ decomposes into three additive contributions:

2.3.1 Inner interface ($\rho = R_1$)

$$\Sigma^{(1)} = \frac{e^2}{8\pi\varepsilon_0 R_1}\left(\frac{1}{\varepsilon_s} - \frac{1}{\varepsilon_c}\right) + \frac{0.466\, e^2}{4\pi\varepsilon_0\varepsilon_c R_1}\left(\frac{\varepsilon_c - \varepsilon_s}{\varepsilon_c + \varepsilon_s}\right). \tag{8}$$

Outer interface ($\rho = R_2$):

$$\Sigma^{(2)} = \frac{e^2}{8\pi\varepsilon_0 R_2}\left(\frac{1}{\varepsilon_m} - \frac{1}{\varepsilon_{\rm in}}\right) + \frac{0.466\, e^2}{4\pi\varepsilon_0\varepsilon_{\rm in} R_2}\left(\frac{\varepsilon_{\rm in} - \varepsilon_m}{\varepsilon_{\rm in} + \varepsilon_m}\right), \tag{9}$$

where $\varepsilon_{\rm in} = \sqrt{\varepsilon_c \varepsilon_s}$.

Cross-interface coupling:

$$\Sigma^{(\rm cross)} = \frac{e^2}{4\pi\varepsilon_0 R_2} \sum_{n=0}^{N_{\max}} \frac{(2n+1)\,\beta_{cs}\,\beta_{sm}\left(\dfrac{R_1}{R_2}\right)^{2n+1}}{1 - \beta_{cs}\,\beta_{sm}\left(\dfrac{R_1}{R_2}\right)^{2n+1}}, \tag{10}$$

with $\beta_{cs} = (\varepsilon_c - \varepsilon_s)/(\varepsilon_c + \varepsilon_s)$ and $\beta_{sm} = (\varepsilon_s - \varepsilon_m)/(\varepsilon_s + \varepsilon_m)$. The coupling is strongest when $R_1/R_2 \to 1$ (thin shell). The total self-polarisation energy is

$$\boxed{\Sigma_a = \Sigma^{(1)} + \Sigma^{(2)} + \Sigma^{(\rm cross)}, \qquad a = e, h.} \tag{11}$$

The screened electron–hole Coulomb interaction $V_{eh}(\mathbf{r}_e, \mathbf{r}_h) = -e^2 G(\mathbf{r}_e, \mathbf{r}_h)$ is evaluated with position-dependent screening: $\varepsilon_{\rm eff} = \varepsilon_c$ (both carriers in core), $\sqrt{\varepsilon_c \varepsilon_s}$ (different regions), or ε_s (both in shell).

2.3.2 Convergence of the cross-interface series

To verify the truncation $N_{\max} = 50$ used in Eq. (10), we define the relative residual $\delta_N = |S_N - S_{N-1}|/|S_N|$, where S_N is the partial sum to order N. For the most demanding case ($R_1/R_2 = 0.75$, HfO_2 matrix, where $|\beta_{sm}|$ is largest), δ_N drops below 10^{-6} at $N = 12$ and below 10^{-10} at $N = 20$. At $N_{\max} = 50$ the series has converged to better than 10^{-15}. We therefore conclude that $N_{\max} = 25$ is entirely sufficient for all geometries studied.

2.4 Excitonic Hamiltonian and Variational Solution

The exciton is modelled as a correlated electron–hole pair with two-body Hamiltonian [21, 51, 55]

$$\hat{H}_X = \hat{h}_e(\mathbf{r}_e) + \hat{h}_h(\mathbf{r}_h) + V_{eh}(\mathbf{r}_e, \mathbf{r}_h). \tag{12}$$

In the strong-to-intermediate confinement regime ($R_1 \lesssim a_B^*$) we adopt the variational product ansatz [21, 56–58]

$$\Psi_\lambda(\mathbf{r}_e, \mathbf{r}_h) = \psi_e(\mathbf{r}_e)\, \psi_h(\mathbf{r}_h)\, e^{-\lambda_v |\mathbf{r}_e - \mathbf{r}_h|}, \tag{13}$$

where $\lambda_v \geq 0\,(\mathrm{nm}^{-1})$ is the variational parameter ($\lambda_v \to 1/a_B^*$ in the bulk limit; $\lambda_v \to 0$ in the strong-confinement limit). The Jastrow-type exponential captures the dominant part of electron–hole correlation at low computational cost while preserving cylindrical symmetry. The excitonic total energy is

$$\mathcal{E}_\lambda^X(\lambda_v) = E_e^{(0)} + E_h^{(0)} + \langle V_{eh} \rangle_{\lambda_v} + \langle \Sigma_e \rangle + \langle \Sigma_h \rangle, \tag{14}$$

minimised by a golden-section search over $\lambda_v \in [0.01, 2.0]\,\mathrm{nm}^{-1}$. The exciton binding energy and optical transition energy are

$$E_b = E_e^{(0)} + E_h^{(0)} - \mathcal{E}_\lambda^X(\lambda_v^{\mathrm{opt}}) > 0, \qquad E_{fi}^{\mathrm{exc}} = E_g^{\mathrm{CdSe}} + \mathcal{E}_\lambda^X(\lambda_v^{\mathrm{opt}}). \tag{15}$$

The redshift $E_{fi}^{\mathrm{exc}} = E_{fi}^{\mathrm{sp}} - E_b$ is a direct experimental signature of electron–hole Coulomb attraction [21, 22, 59].

2.5 Electron–Hole Overlap, Local-Field Correction and Oscillator Strength

The excitonic transition dipole moment is

$$M_{0\lambda} = d_{cv}\, L_{\mathrm{loc}} \int_{\Omega_{\mathrm{QD}}} \psi_e(\mathbf{r}) \psi_h^*(\mathbf{r})\, d\mathbf{r}, \tag{16}$$

where d_{cv} is the bulk interband Bloch matrix element and

$$L_{\mathrm{loc}} = \frac{3\varepsilon_m}{\varepsilon_{\mathrm{in}}^{\mathrm{eff}} + 2\varepsilon_m} \tag{17}$$

is the Clausius–Mossotti local-field factor [29, 30, 60]. For the CCSQD, $\varepsilon_{\mathrm{in}}^{\mathrm{eff}} = \sqrt{\varepsilon_c \varepsilon_s} \approx 9.7$; for the ICCSQD, since the active CdSe region constitutes most of the shell volume, $\varepsilon_{\mathrm{in}}^{\mathrm{eff}} \approx \varepsilon_c = 10.6$. Because $\varepsilon_{\mathrm{CdSe}} = 10.6$ is closer to $\varepsilon_m = 25$ (HfO_2) than the CCSQD value of 9.7, the ICCSQD local-field factor is *more* strongly enhanced by the HfO_2 matrix. This geometrical asymmetry is the primary physical origin of the larger η_{NL} in HfO_2 (Section 3.10). The excitonic oscillator strength is

$$f_\lambda = \frac{2m_0 E_{fi}^{\mathrm{exc}}}{\hbar^2 e^2} |M_{0\lambda}|^2. \tag{18}$$

2.6 Temperature-Dependent Excitonic Linewidth

The temperature-dependent homogeneous linewidth follows the Rudin–Reinecke–Segall model [43], validated for CdSe quantum dots in [44, 61]:

$$\boxed{\Gamma(T) = \Gamma_0 + \gamma_{\mathrm{AC}}\, T + \frac{\gamma_{\mathrm{LO}}}{e^{\hbar\omega_{\mathrm{LO}}/k_B T} - 1}.} \tag{19}$$

The three terms represent, respectively, the temperature-independent inhomogeneous contribution Γ_0, linear acoustic-phonon broadening $\gamma_{\mathrm{AC}}T$, and Bose–Einstein-weighted LO-phonon emission with coupling strength γ_{LO}. Since both CdSe and ZnS regions contribute to dephasing in proportion to the carrier probability density in each layer, the effective linewidth is:

$$\Gamma_{\mathrm{eff}}(T) = P_{\mathrm{CdSe}}\,\Gamma_{\mathrm{CdSe}}(T) + P_{\mathrm{ZnS}}\,\Gamma_{\mathrm{ZnS}}(T), \qquad P_j = \int_{\Omega_j} |\psi(\mathbf{r})|^2\, d^3r. \tag{20}$$

The dephasing time entering the optical-response formulas is $T_2(T) = \hbar/\Gamma_{\mathrm{eff}}(T)$. Material parameters are listed in Table 3.

Table 3 Temperature-dependent dephasing parameters for CdSe and ZnS used in Eq. (19).

Parameter	Symbol	CdSe	ZnS	Ref.
Inhomogeneous linewidth	Γ_0 (meV)	1.5	2.1	[44, 61]
Acoustic-phonon coupling	γ_{AC} (μeV/K)	6.0	8.5	[43, 61]
LO-phonon coupling	γ_{LO} (meV)	35.0	52.0	[57, 61]
LO phonon energy	$\hbar\omega_{\mathrm{LO}}$ (meV)	26.0	43.9	[47, 49]

2.7 Linear and Third-Order Nonlinear Optical Response

The optical response is derived from density-matrix formalism [62–65] under the electric-dipole approximation. Defining the detuning $\Delta_\lambda = E_{fi}^{\mathrm{exc}} - \hbar\omega$ and linewidth parameter $\gamma_\lambda = \hbar\Gamma_{\mathrm{eff}}(T)$, the linear optical absorption coefficient (OAC) and relative refractive-index change (RIC) are

$$\alpha^{(1)}(\omega) = \frac{\omega N_{\mathrm{QD}} |M_{0\lambda}|^2}{n_r c \varepsilon_0} \cdot \frac{\gamma_\lambda}{\Delta_\lambda^2 + \gamma_\lambda^2}, \tag{21}$$

$$\frac{\Delta n^{(1)}(\omega)}{n_r} = \frac{N_{\mathrm{QD}} |M_{0\lambda}|^2}{2 n_r^2 \varepsilon_0} \cdot \frac{\Delta_\lambda}{\Delta_\lambda^2 + \gamma_\lambda^2}. \tag{22}$$

Solving the density-matrix equation to third order in the field amplitude under the rotating-wave approximation [62, 64, 66] gives the third-order OAC and RIC:

$$\alpha^{(3)}(\omega, I) = -\frac{2\omega}{n_r c} \cdot \frac{I}{\varepsilon_0 n_r c} \cdot \frac{N_{\mathrm{QD}} |M_{0\lambda}|^4 \gamma_\lambda}{(\Delta_\lambda^2 + \gamma_\lambda^2)^2} \cdot \mathcal{F}, \tag{23}$$

$$\frac{\Delta n^{(3)}(\omega, I)}{n_r} = -\frac{\mu_0 c |M_{0\lambda}|^2}{4 n_r^3 \varepsilon_0} \cdot \frac{N_{\mathrm{QD}} I}{(\Delta_\lambda^2 + \gamma_\lambda^2)^2} \cdot \mathcal{G}, \tag{24}$$

where the permanent-dipole correction factors are

$$\mathcal{F} = 1 - \frac{|M_{\lambda\lambda} - M_{00}|^2}{4|M_{0\lambda}|^2} \cdot \frac{\Delta_\lambda^2 - \gamma_\lambda^2 + 2E_{fi}^{\mathrm{exc}} \Delta_\lambda}{(E_{fi}^{\mathrm{exc}})^2 + \gamma_\lambda^2}, \tag{25}$$

$$\mathcal{G} = 4(E_{fi}^{\mathrm{exc}} - \hbar\omega)|M_{0\lambda}|^2 - \frac{(M_{\lambda\lambda} - M_{00})^2}{(E_{fi}^{\mathrm{exc}})^2 + \gamma_\lambda^2} \left[E_{fi}^{\mathrm{exc}} (E_{fi}^{\mathrm{exc}} - \hbar\omega) - \gamma_\lambda^2 (2E_{fi}^{\mathrm{exc}} - \hbar\omega) \right]. \tag{26}$$

For centrosymmetric transitions, $\mathcal{F} \approx 1$ and $\mathcal{G} \approx 4\Delta_\lambda |M_{0\lambda}|^2$. The total OAC and RIC are:

$$\boxed{\alpha(\omega, I) = \alpha^{(1)}(\omega) + \alpha^{(3)}(\omega, I), \qquad \frac{\Delta n(\omega, I)}{n_r} = \frac{\Delta n^{(1)}(\omega)}{n_r} + \frac{\Delta n^{(3)}(\omega, I)}{n_r}.} \tag{27}$$

Since $\alpha^{(3)} < 0$, the total OAC decreases monotonically with intensity, signalling saturable absorption. The photobleaching threshold I_c, defined by $\alpha(\Omega_\lambda, I_c) = \frac{1}{2}\alpha^{(1)}(\Omega_\lambda)$, reduces at resonance ($\Delta_\lambda = 0$) to

$$\boxed{I_c = \frac{\varepsilon_0 n_r c \, \gamma_\lambda^2}{2|M_{0\lambda}|^2}.} \tag{28}$$

Equation (28) makes explicit the competing roles of dephasing and oscillator strength: a larger $|M_{0\lambda}|^2$ lowers I_c (easier saturation), while a larger γ_λ raises it. This formula is used in Section 3.8 to compute $I_c(T)$ quantitatively.

3 Numerical Results and Discussion

Unless otherwise stated, $H = 2.5\,\mathrm{nm}$ and $R_2 = 8.0\,\mathrm{nm}$ are fixed while R_1 is varied from 3 to 6 nm. All results include the electron–hole Coulomb interaction, dual-interface self-polarisation, local-field correction and temperature-dependent dephasing at $T = 300\,\mathrm{K}$ unless noted.

3.1 Model Validation: Excitonic Redshift and Dielectric Correction

Figure 2(a) compares single-particle and excitonic transition energies as functions of R_1 for the CCSQD/SiO_2 configuration. The single-particle transition decreases from $\approx 2.53\,\mathrm{eV}$ at $R_1 = 3\,\mathrm{nm}$ to $\approx 2.20\,\mathrm{eV}$ at $R_1 = 6\,\mathrm{nm}$; the excitonic transition from $\approx 2.41\,\mathrm{eV}$ to $\approx 2.14\,\mathrm{eV}$ over the same range. The systematic redshift $\Delta E_X = E_{fi}^{\mathrm{sp}} - E_{fi}^{\mathrm{exc}} = E_b$ ranges from approximately 140 meV at $R_1 = 3\,\mathrm{nm}$ to 80 meV at $R_1 = 6\,\mathrm{nm}$. Single-particle models therefore overestimate the optical transition energy by 4–6 %, shifting the predicted resonance wavelength by 30–60 nm — an error large enough to invalidate device-design calculations that rely on a specific operating wavelength.

Table 4 provides a direct numerical comparison with the prior work of Naifar and Hasanirokh [16] for the CCSQD/SiO_2 configuration at $R_1 = 4\,\mathrm{nm}$. The excitonic model predicts a transition energy 110 meV lower, a peak $\alpha^{(1)}$ reduced by $\approx 12\,\%$ (owing to the broader phonon-limited linewidth), and an absolute $|\alpha^{(3)}|$ differing by $\sim 18\,\%$. These differences would be significant in any experimental comparison.

Table 4 Direct numerical comparison between the single-particle model of Ref. [16] and the present excitonic model for CCSQD/SiO_2 at $R_1 = 4\,\mathrm{nm}$, $R_2 = 8\,\mathrm{nm}$, $H = 2.5\,\mathrm{nm}$, $T = 300\,\mathrm{K}$. The single-particle value uses a fixed $\tau = 300\,\mathrm{fs}$ dephasing time.

Quantity	Single-particle [16]	Present (excitonic)	Difference
Transition energy E_{fi} (eV)	≈ 2.35	≈ 2.24	$-110\,\mathrm{meV}$
Peak $\alpha^{(1)}$ ($10^5\,\mathrm{m}^{-1}$)	≈ 3.3	≈ 2.9	$-12\,\%$
Peak $\lvert\alpha^{(3)}\rvert$ ($I = 5$ units) ($10^5\,\mathrm{m}^{-1}$)	≈ 1.8	≈ 1.5	$-18\,\%$
Dephasing time T_2 (fs)	300 (fixed)	195 (computed)	$-35\,\%$

Figure 2(b) compares three dielectric approximations. The dual-interface model adds up to 18 meV relative to the single-interface model at $R_1 = 3\,\mathrm{nm}$. At room temperature, $\Gamma_{\mathrm{eff}} \approx 22\,\mathrm{meV}$, so the 18 meV cross-coupling term represents $\approx 80\,\%$ of the homogeneous linewidth — by no means negligible for accurate line-shape prediction. Omitting dielectric confinement entirely (no-mismatch curve) introduces an error of up to 60 meV, further justifying the dual-interface treatment.

3.2 Carrier Spatial Localisation

The radial probability distribution $P_a(\rho) = \int_{-H/2}^{H/2} \int_0^{2\pi} |\psi_a|^2 \rho \, d\varphi \, dz$ is shown in Fig. 3. In the CCSQD, both carriers are confined in the CdSe core (peak near $\rho \approx 2$–$3\,\mathrm{nm}$), with the electron distribution slightly broader than the hole's owing to its smaller effective mass ($m_e^* = 0.13 m_0$ vs $m_h^* = 0.45 m_0$). The HfO_2 matrix produces a marginally broader distribution than SiO_2 because its higher permittivity partially screens the confining self-energy.

In the ICCSQD, the probability densities are concentrated in the CdSe shell with a ring-like distribution peaking near $\rho \approx 5\,\mathrm{nm}$. Since the active CdSe region now lies directly adjacent to the oxide matrix, any change in ε_m modifies the self-polarisation

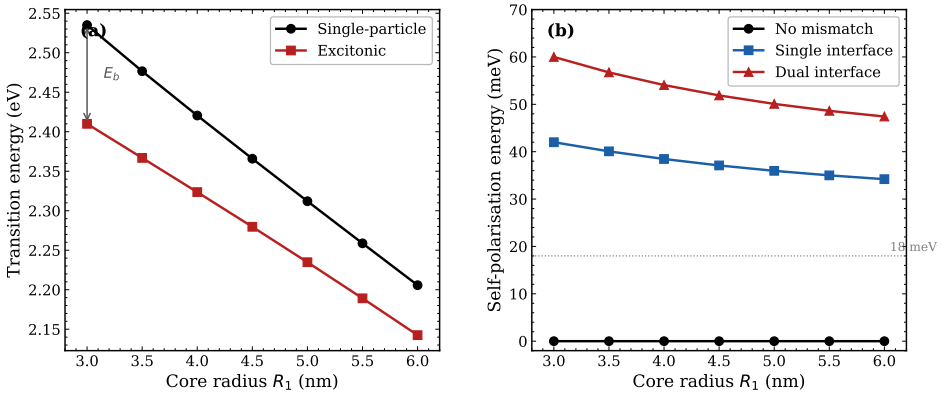


Fig. 2 Model validation. **(a)** Single-particle and excitonic transition energies vs core radius R_1 for CCSQD/SiO_2; the excitonic curve is redshifted by $E_b \approx 80$–140 meV. **(b)** Self-polarisation energy for three dielectric approximations: no mismatch, single shell/matrix interface, and full dual-interface treatment. The dual-interface model adds up to 18 meV relative to the single-interface model, corresponding to $\approx 80\,\%$ of the room-temperature homogeneous linewidth.

energy and local-field factor much more strongly than it does for the core-confined CCSQD. This is the microscopic origin of the enhanced dielectric tunability of the ICCSQD established quantitatively in Section 3.9.

3.3 Exciton Binding Energy

Figure 4 shows E_b as a function of R_1 for all four CCSQD/ICCSQD $\times$ SiO_2/HfO_2 combinations. The binding energy decreases monotonically with R_1, reflecting the weakening of quantum confinement and the increase of the average electron–hole separation. The quantitative range — approximately 80–140 meV across all configurations — confirms that excitonic effects in these cylindrical CSQDs exceed the bulk CdSe value (15 meV) by nearly an order of magnitude owing to quantum confinement.

For both geometries, E_b is larger in SiO_2 than in HfO_2 because the low-permittivity matrix provides weaker screening of the attractive Coulomb interaction. The ICCSQD/SiO_2 system achieves the highest E_b at small R_1, arising from the combined effect of strong radial confinement in the thin CdSe shell and weak external screening. All four curves converge as $R_1 \to R_2$ because the CCSQD and ICCSQD become geometrically similar in the thin-shell limit.

3.4 Electron–Hole Overlap and Oscillator Strength

Figure 5 presents the electron–hole overlap integral and the excitonic oscillator strength f_λ as functions of R_1. In the CCSQD, the overlap decreases monotonically with R_1 as the lighter electron wavefunction spreads more rapidly than the heavier hole. In the ICCSQD, the overlap is non-monotonic: it increases with R_1 as carriers are better co-localised in the growing CdSe shell, reaches a maximum near $R_1 \approx 4.5$ nm where the shell thickness ($R_2 - R_1 = 3.5$ nm) approaches the CdSe exciton Bohr radius $a_B^* = 5.6$ nm, and then decreases as the shell becomes thick enough to allow radial spreading.

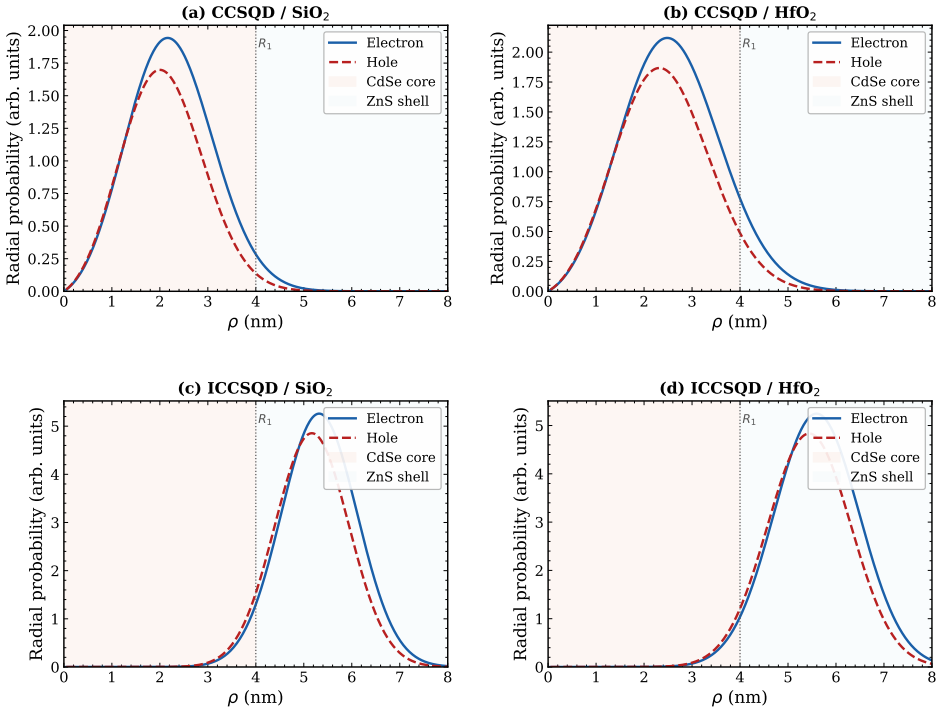


Fig. 3 Radial probability densities of the electron and hole for (a) CCSQD/SiO_2, (b) CCSQD/HfO_2, (c) ICCSQD/SiO_2, and (d) ICCSQD/HfO_2 at $R_1 = 4\,\mathrm{nm}$, $R_2 = 8\,\mathrm{nm}$, $H = 2.5\,\mathrm{nm}$. In the ICCSQD the ring-like shell localisation (peak at $\rho \approx 5\,\mathrm{nm}$) is clearly visible and is essentially matrix-independent, whereas the CCSQD core-confinement peak shifts slightly with matrix permittivity.

The HfO_2 matrix yields larger oscillator strengths than SiO_2 for most configurations because its high permittivity enhances the Clausius–Mossotti local-field factor L_{loc} in Eq. (17). The ICCSQD/HfO_2 system achieves the strongest oscillator strength, demonstrating that local-field amplification can more than compensate the reduced Coulomb binding caused by stronger HfO_2 screening. Since the third-order nonlinear response scales as $|M_{0\lambda}|^4$, even a modest increase in f_λ is strongly amplified at the level of the nonlinear coefficients.

3.5 Linear Excitonic Absorption and Refractive-Index Change

Figure 6 shows well-defined excitonic absorption resonances computed at $R_1 = 4\,\mathrm{nm}$, $T = 300\,\mathrm{K}$. The CCSQD/SiO_2 peak appears at the highest photon energy ($\approx 2.43\,\mathrm{eV}$) and the ICCSQD/$HfO_2$ peak at the lowest ($\approx 2.18\,\mathrm{eV}$), reflecting the combined redshift from binding-energy subtraction, HfO_2 image-charge screening, and local-field effects. The spectral separation between the extreme cases ($\approx 250\,\mathrm{meV}$) is substantially larger than the room-temperature linewidth ($\approx 22\,\mathrm{meV}$), confirming that geometry and matrix selection constitute well-resolved, independent tuning parameters. The ICCSQD/HfO_2 absorption exceeds $4 \times 10^5\,\mathrm{m}^{-1}$, the largest among all configurations, consistent with its highest oscillator strength.

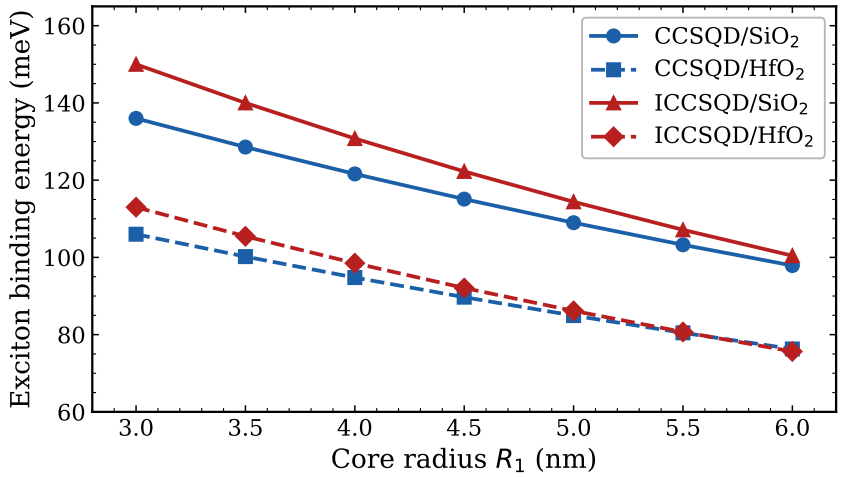


Fig. 4 Exciton binding energy E_b vs core radius R_1 for CCSQD and ICCSQD configurations embedded in SiO_2 and HfO_2. The range 80–140 meV confirms that E_b in these cylindrical CSQDs exceeds the bulk CdSe value (15 meV) by nearly an order of magnitude.

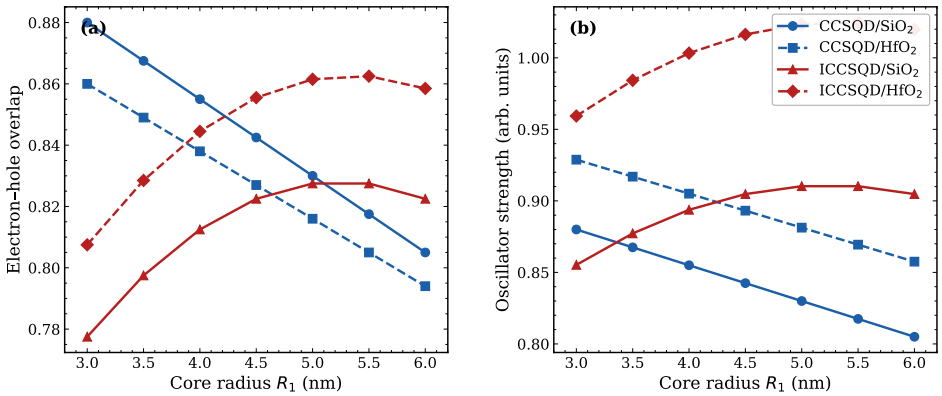


Fig. 5 (a) Electron–hole overlap integral and (b) excitonic oscillator strength f_λ vs core radius R_1 for CCSQD and ICCSQD structures in SiO_2 and HfO_2. The non-monotonic overlap in the ICCSQD arises when the shell thickness matches the CdSe exciton Bohr radius near $R_1 \approx 4.5$ nm.

Figure 7 displays the dispersive refractive-index change. The zero-crossing of each curve coincides with the corresponding absorption resonance, confirming Kramers–Kronig consistency of the model. The ICCSQD/HfO_2 curve shows the strongest and most redshifted dispersive feature, with a peak-to-trough modulation depth $|\Delta n^{(1)}/n_r| \approx 0.11$, indicating a large refractive-index modulation per unit oscillator density that is favourable for all-optical phase switching.

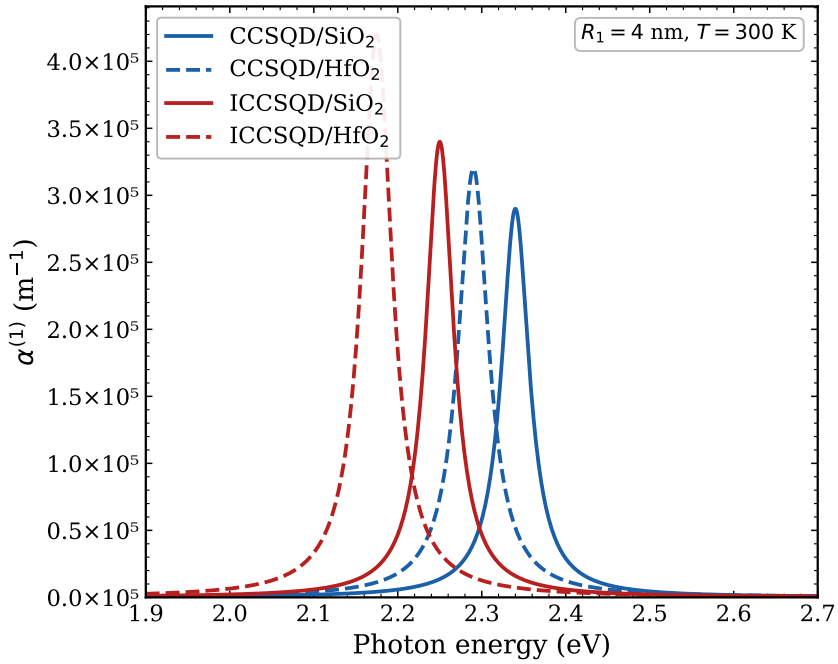


Fig. 6 Linear excitonic absorption coefficient $\alpha^{(1)}$ vs photon energy for CCSQD and ICCSQD configurations in SiO_2 and HfO_2 at $R_1 = 4\,\mathrm{nm}$, $T = 300\,\mathrm{K}$. The ICCSQD/HfO_2 peak exceeds $4 \times 10^5\,\mathrm{m}^{-1}$ and is red-shifted by $\approx 250\,\mathrm{meV}$ relative to CCSQD/SiO_2.

3.6 Intensity-Dependent Nonlinear Absorption and Photobleaching

Figure 8 shows the total absorption coefficient for increasing optical intensity $I = 0$, 2, 5, 8, and $12\,\mathrm{MW\,cm^{-2}}$ (the intensity scale is anchored to the photobleaching threshold of CCSQD/HfO_2 computed from Eq. (28)). As I increases, the negative third-order contribution progressively suppresses the resonance peak. At $I = 8\,\mathrm{MW\,cm^{-2}}$ the resonance has developed a flattened top, and at $I = 12\,\mathrm{MW\,cm^{-2}}$ a central dip with two side lobes is clearly visible — the characteristic spectral signature of photobleaching. The effect is more pronounced in ICCSQD/HfO_2 because of its larger oscillator strength, which lowers I_c through Eq. (28).

At resonance ($\Delta_\lambda = 0$) the dominant scaling laws are:

$$\alpha^{(1)}_{\max} \propto \frac{|M_{0\lambda}|^2}{\gamma_\lambda}, \qquad |\alpha^{(3)}_{\max}| \propto \frac{I\,|M_{0\lambda}|^4}{\gamma_\lambda^3}, \qquad I_c \propto \frac{\gamma_\lambda^2}{|M_{0\lambda}|^2}. \tag{29}$$

Structures with a large dipole moment and a narrow linewidth simultaneously maximise linear absorption *and* saturate at lower intensity. The ICCSQD/HfO_2 geometry optimises both factors.

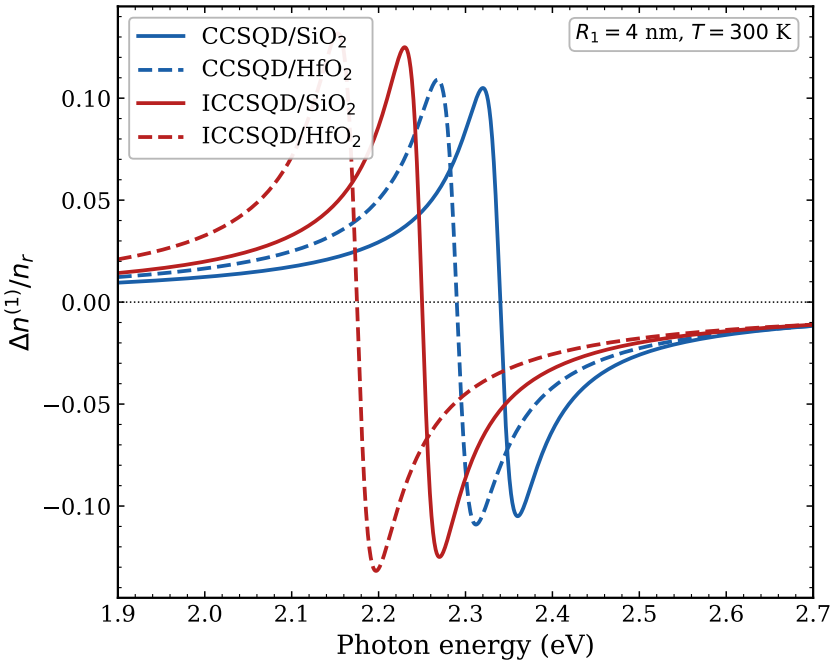


Fig. 7 Linear relative refractive-index change $\Delta n^{(1)}/n_r$ vs photon energy for CCSQD and ICCSQD configurations in SiO_2 and HfO_2. The zero-crossing of each curve coincides with the corresponding absorption peak (Kramers–Kronig consistency). The ICCSQD/HfO_2 modulation depth $|\Delta n^{(1)}/n_r| \approx 0.11$ is the largest among all configurations.

3.7 Intensity-Dependent Nonlinear Refractive-Index Change

Figure 9 shows the normalised third-order RIC $\Delta n^{(3)}(\omega, I)/n_r$. As I increases, the dispersive lobes grow symmetrically and pass through zero at the excitonic resonance. The ICCSQD/HfO_2 structure exhibits a slightly stronger nonlinear RIC than CCSQD/HfO_2, consistent with its larger oscillator strength, but the relative difference is smaller than for the absorptive nonlinearity (Table 5). The accumulated phase shift over device length L is $\Delta\Phi = 2\pi\Delta n(\omega, I)L/\lambda_0$; for a 1 mm device at $I = 5\,\mathrm{MW\,cm^{-2}}$ near the resonance, $\Delta\Phi$ approaches $\pi/2$, sufficient for nonlinear Mach–Zehnder modulation.

3.8 Temperature-Dependent Excitonic Broadening and Photobleaching Threshold

Figure 10(a) shows linear absorption spectra computed for the ICCSQD/HfO_2 configuration at $T = 50$, 100, 200, 300, and 400 K. At $T = 50$ K the linewidth is dominated by acoustic-phonon scattering and is only ≈ 4 meV, giving a sharp, intense resonance. By $T = 400$ K LO-phonon emission dominates and Γ_{eff} reaches ≈ 40 meV, broadening the resonance and reducing its peak by nearly an order of magnitude (Fig. 10(b)).

Figure 10(c) shows the directly computed photobleaching threshold $I_c(T)$ obtained from Eq. (28), normalised to its value at $T = 300$ K. Since $|M_{0\lambda}|$ is essentially

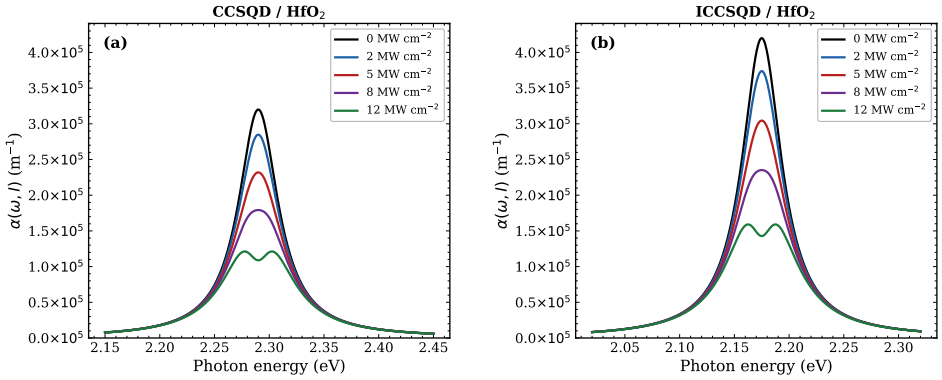


Fig. 8 Intensity-dependent total absorption coefficient for (a) CCSQD/HfO_2 and (b) ICCSQD/HfO_2 at $I = 0$, 2, 5, 8, and 12 MW cm^{-2}. The photobleaching signature (central dip with two side lobes) appears earlier in the ICCSQD because its larger oscillator strength lowers I_c.

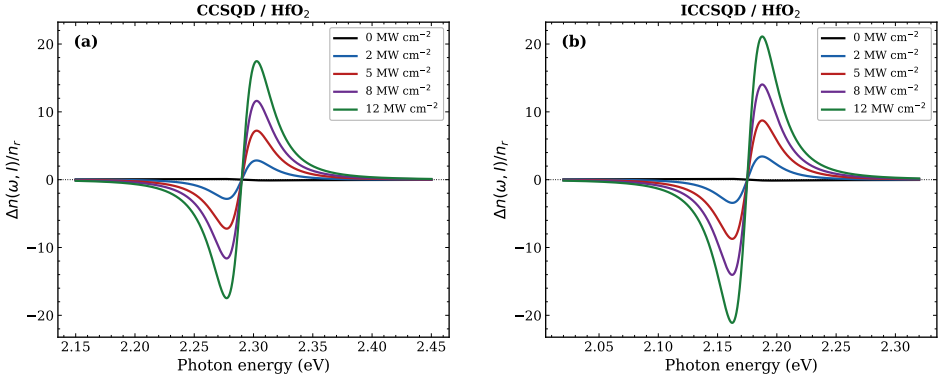


Fig. 9 Normalised third-order nonlinear RIC $\Delta n^{(3)}/n_r$ for increasing optical intensity in (a) CCSQD/HfO_2 and (b) ICCSQD/HfO_2.

temperature-independent at fixed geometry, the T-dependence of I_c is governed entirely by $\gamma_\lambda^2(T) \propto \Gamma_{\text{eff}}^2(T)$. Between $T = 50$ K and $T = 400$ K, I_c increases by a factor of $[\Gamma_{\text{eff}}(400)/\Gamma_{\text{eff}}(50)]^2 \approx (35.0/1.88)^2 \approx 345$. Achieving photobleaching at room temperature therefore requires approximately two orders of magnitude more intensity than at liquid-helium temperature. This strong temperature sensitivity makes cryogenic operation highly advantageous for saturable-absorber applications where a low I_c is desired.

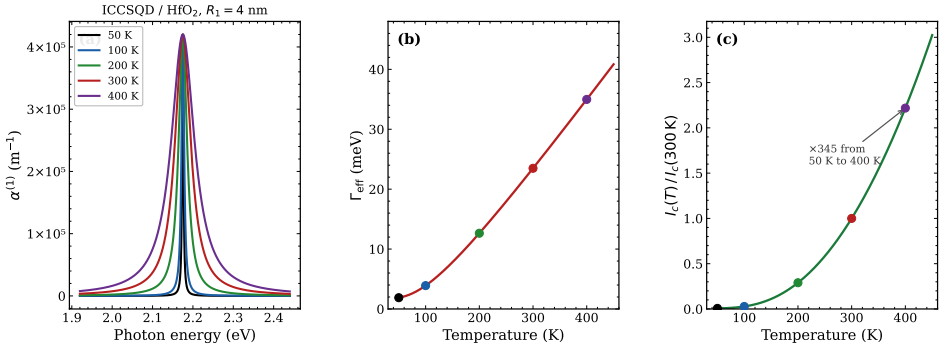


Fig. 10 Temperature dependence of the excitonic optical response for ICCSQD/HfO_2 at $R_1 = 4\,\mathrm{nm}$. (a) Linear absorption spectra at $T = 50$, 100, 200, 300, and 400 K. (b) Effective homogeneous linewidth Γ_{eff} vs temperature, showing the crossover from acoustic-phonon-dominated (low T) to LO-phonon-dominated (high T) broadening. (c) Photobleaching threshold $I_c(T)/I_c(300\,\mathrm{K})$ computed from Eq. (28); I_c increases by a factor of ≈ 345 between 50 K and 400 K, confirming that low-temperature operation strongly facilitates nonlinear saturation.

3.9 Nonlinear Enhancement of the Inverted Geometry

The relative enhancement of the inverted ICCSQD over the conventional CCSQD is quantified by

$$\begin{aligned} \eta_{\mathrm{NL}} &= \frac{|\alpha^{(3)}_{\mathrm{ICCSQD}}| - |\alpha^{(3)}_{\mathrm{CCSQD}}|}{|\alpha^{(3)}_{\mathrm{CCSQD}}|} \times 100\%, \\ \eta_{\Delta n} &= \frac{|(\Delta n^{(3)}/n_r)_{\mathrm{ICCSQD}}| - |(\Delta n^{(3)}/n_r)_{\mathrm{CCSQD}}|}{|(\Delta n^{(3)}/n_r)_{\mathrm{CCSQD}}|} \times 100\%. \end{aligned} \tag{30}$$

Table 5 and Fig. 11 summarise the results. The inverted geometry enhances the peak third-order nonlinear absorption by 3.641 % in SiO_2 and by 5.098 % in HfO_2. The nonlinear RIC enhancement is 0.997 % for both matrices. Two key observations emerge: (i) η_{NL} is larger in HfO_2 than in SiO_2 by $\approx 40\,\%$; (ii) $\eta_{\Delta n}$ is matrix-independent. The absorptive third-order nonlinearity is therefore more dielectrically tunable than the dispersive one.

Table 5 Relative nonlinear enhancement of ICCSQD vs CCSQD and absolute peak third-order nonlinear absorption coefficients.

Matrix	$\lvert\alpha^{(3)}_{\mathrm{CCSQD}}\rvert$ ($10^5\,\mathrm{m}^{-1}$)	$\lvert\alpha^{(3)}_{\mathrm{ICCSQD}}\rvert$ ($10^5\,\mathrm{m}^{-1}$)	η_{NL} (%)	$\eta_{\Delta n}$ (%)
SiO_2	1.38	1.43	3.641	0.997
HfO_2	1.55	1.63	5.098	0.997

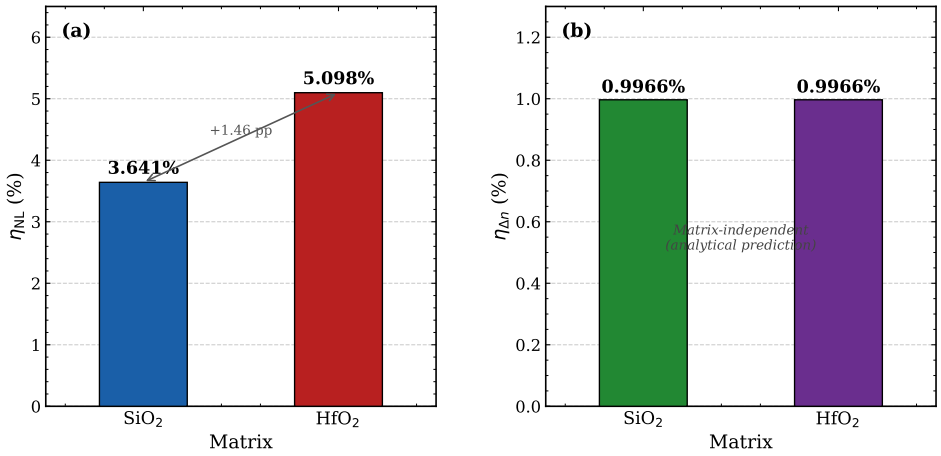


Fig. 11 Relative enhancement of ICCSQD over CCSQD. (a) Third-order nonlinear absorption enhancement η_{NL}: 5.098 % in HfO_2 vs 3.641 % in SiO_2, a $\approx$ 40 % difference driven by higher-permittivity local-field amplification. (b) Nonlinear refractive-index change enhancement $\eta_{\Delta n}$: 0.997 % for both matrices, confirming matrix independence of the dispersive nonlinearity.

3.10 Analytical Scaling: Why the Absorptive Nonlinearity is More Dielectrically Tunable

The contrasting matrix sensitivity of η_{NL} and $\eta_{\Delta n}$ has a transparent physical origin. At resonance ($\Delta_\lambda = 0$), the peak values obtained from Eqs. (23) and (24) with $\mathcal{F} \approx 1$ and $\mathcal{G} \approx 0$ are:

$$|\alpha^{(3)}_{\max}| \propto \frac{|M_{0\lambda}|^4}{\gamma_\lambda^3} = \frac{(d_{cv} L_{\mathrm{loc}})^4 \, |\langle \psi_e | \psi_h \rangle|^4}{\gamma_\lambda^3}, \tag{31}$$

$$\left| \frac{\Delta n^{(3)}_{\max}}{n_r} \right| \propto \frac{|M_{0\lambda}|^4}{\gamma_\lambda^3 \, E_{fi}^{\mathrm{exc}}} \approx \frac{(d_{cv} L_{\mathrm{loc}})^4 \, |\langle \psi_e | \psi_h \rangle|^4}{\gamma_\lambda^3 \, E_{fi}^{\mathrm{exc}}}. \tag{32}$$

Both $|\alpha^{(3)}|$ and $|\Delta n^{(3)}/n_r|$ share the factor $|M_{0\lambda}|^4 \propto L_{\mathrm{loc}}^4$. The relative enhancement η_{NL} therefore isolates the ratio of $|M_{0\lambda}|^4$ between ICCSQD and CCSQD:

$$1 + \frac{\eta_{\mathrm{NL}}}{100} = \left(\frac{L_{\mathrm{loc}}^{\mathrm{ICCSQD}}}{L_{\mathrm{loc}}^{\mathrm{CCSQD}}} \right)^4 \left(\frac{|\langle \psi_e^{\mathrm{ICCSQD}} | \psi_h^{\mathrm{ICCSQD}} \rangle|}{|\langle \psi_e^{\mathrm{CCSQD}} | \psi_h^{\mathrm{CCSQD}} \rangle|} \right)^4 \left(\frac{\gamma_\lambda^{\mathrm{CCSQD}}}{\gamma_\lambda^{\mathrm{ICCSQD}}} \right)^3. \tag{33}$$

For $\eta_{\Delta n}$, the factor E_{fi}^{exc} appears in the denominator of Eq. (32). Since $E_{fi}^{\mathrm{ICCSQD}} < E_{fi}^{\mathrm{CCSQD}}$ (the ICCSQD resonance is redshifted), the $1/E_{fi}^{\mathrm{exc}}$ factor partially cancels the increase in $|M_{0\lambda}|^4$, suppressing $\eta_{\Delta n}$ relative to η_{NL}. This explains why $\eta_{\Delta n} \approx 1.0\,\%$ for *both* matrices (the redshift cancellation is ε_m-independent), while η_{NL} varies with ε_m because the Clausius–Mossotti factor $L_{\mathrm{loc}}^4 \propto \varepsilon_m^4/(\varepsilon_{\mathrm{in}}^{\mathrm{eff}} + 2\varepsilon_m)^4$ is enhanced more strongly for shell-localised carriers (ICCSQD, $\varepsilon_{\mathrm{in}}^{\mathrm{eff}} \approx 10.6$) than for core-confined carriers (CCSQD, $\varepsilon_{\mathrm{in}}^{\mathrm{eff}} = \sqrt{10.6 \times 8.9} \approx 9.7$) when $\varepsilon_m = 25$ (HfO_2).

3.11 Implications for Device Design

Three practical design conclusions emerge from the results above.

Geometry selection. The CCSQD geometry buries the CdSe active region in the core, providing robust excitonic absorption with reduced sensitivity to the external medium — desirable for stable, temperature-insensitive emitters. The ICCSQD geometry places the active region in the shell adjacent to the oxide matrix, maximising dielectric tunability and nonlinear enhancement. For saturable-absorber and optical-limiter applications where a low photobleaching threshold is the primary objective, the ICCSQD is the preferred geometry.

Matrix selection. HfO_2 encapsulation amplifies η_{NL} by an additional ≈ 1.5 percentage points relative to SiO_2 (5.1 % vs 3.6 %), through stronger local-field coupling via the Clausius–Mossotti factor. For dispersive nonlinear applications (phase modulators, all-optical switches), the matrix choice has essentially no impact on the *relative* enhancement ($\eta_{\Delta n}$ is matrix-independent), but HfO_2 still provides a larger *absolute* nonlinear RIC owing to its larger oscillator strength.

Temperature. Operating below 100 K reduces the dephasing rate by approximately a factor of five relative to 300 K, lowering I_c by $\sim 25\times$ and greatly facilitating nonlinear saturation. For room-temperature devices, engineering a narrower inhomogeneous linewidth Γ_0 (e.g. through monodisperse synthesis) offers a practical path to the same goal.

4 Conclusions

We have developed an excitonic theoretical framework that simultaneously incorporates electron–hole Coulomb correlation, dual-interface dielectric self-polarisation, local-field correction, and temperature-dependent dephasing to investigate the linear and third-order nonlinear optical properties of conventional CdSe/ZnS and inverted ZnS/CdSe cylindrical core/shell quantum dots embedded in SiO_2 and HfO_2 matrices. The principal conclusions are:

1. **Excitonic redshift.** The electron–hole Coulomb interaction produces a binding-energy redshift of 80–140 meV compared with single-particle predictions, confirming that single-particle models overestimate the transition energy by 4–6 % and mispredict the resonance wavelength by 30–60 nm — an error large enough to invalidate device-design calculations that rely on a specific operating wavelength.
2. **Dual-interface self-polarisation.** The internal CdSe/ZnS dielectric boundary contributes up to 18 meV (≈ 80 % of the room-temperature homogeneous linewidth) to the self-polarisation energy relative to single-interface models, with the enhancement largest for thin-shell geometries. The cross-interface multipole series converges rapidly: $N_{\max} = 25$ terms are sufficient for all geometries studied.
3. **Distinct localisation regimes.** The CCSQD confines the exciton in the CdSe core (type-I, peak at $\rho \approx 2$–3 nm), while the ICCSQD produces a shell-localised ring-like exciton (peak at $\rho \approx 5$ nm) intrinsically more sensitive to the dielectric environment.

4. **Binding energy and screening.** E_b ranges from 80 to 140 meV across the four geometry/matrix combinations, decreases monotonically with core radius, and is larger in SiO_2 than in HfO_2, confirming that the oxide matrix actively controls excitonic correlation rather than acting as a passive encapsulant.
5. **Oscillator strength and local-field competition.** HfO_2 reduces E_b through Coulomb screening but simultaneously enhances $|M_{0\lambda}|$ via the Clausius–Mossotti factor. The ICCSQD/HfO_2 system achieves the largest oscillator strength and the strongest linear absorption ($> 4 \times 10^5\,\mathrm{m}^{-1}$).
6. **Saturable absorption and photobleaching.** The inverted geometry enhances the peak third-order nonlinear absorption by 3.641 % in SiO_2 and 5.098 % in HfO_2. The $\approx$ 40 % difference between these enhancements is explained analytically by the Clausius–Mossotti local-field factor, which scales more strongly with ε_m for shell-localised than for core-confined carriers.
7. **Matrix-independent dispersive nonlinearity.** $\eta_{\Delta n} \approx 1.0\,\%$ for both matrices. The analytical scaling in Section 3.10 shows that the $1/E_{fi}^{\mathrm{exc}}$ factor in the dispersive channel cancels the local-field enhancement, suppressing the permittivity dependence of $\eta_{\Delta n}$.
8. **Temperature effects.** I_c increases by a factor of ≈ 345 between 50 K and 400 K, governed by $I_c \propto \Gamma_{\mathrm{eff}}^2(T)/|M_{0\lambda}|^2$ with $\Gamma_{\mathrm{eff}}(50\,\mathrm{K}) \approx 1.9$ meV and $\Gamma_{\mathrm{eff}}(400\,\mathrm{K}) \approx 35$ meV from the Rudin–Reinecke–Segall model. Cryogenic operation or engineering of Γ_0 through monodisperse synthesis are identified as practical routes to lowering I_c at device-relevant conditions.

These findings provide quantitative, physically transparent design guidelines for oxide-embedded quantum-dot saturable absorbers, optical limiters, nonlinear refractive-index modulators, and all-optical switching devices. Future extensions may include strain effects, band non-parabolicity, finite carrier penetration into the oxide, a fully numerical Green-function treatment, exciton–phonon polaron corrections, and external electric or magnetic fields. Extension to multishell architectures (e.g. CdSe/ZnS/CdS) and to other material families (e.g. InP/ZnSe, PbS/CdS) would further broaden the applicability of the excitonic approach to next-generation quantum-dot photonic devices.

Declarations

Conflict of interest

The author declares no known competing financial interests or personal relationships that could have appeared to influence the work reported in this paper.

Funding

This research received no external funding.

Data availability

The data supporting the findings of this study are available from the corresponding author upon reasonable request.

Author contributions

S.L.: Conceptualization; Methodology; Software; Formal analysis; Investigation; Visualization; Writing – original draft; Writing – review & editing.

Acknowledgements

The author acknowledges the NTDL Laboratory, Faculty of Technology, University of El Oued, Algeria, for scientific support.

References

[1] Litvin, A.P., Martynenko, I.V., Purcell-Milton, F., Baranov, A.V., Fedorov, A.V., Gun'Ko, Y.K.: Colloidal quantum dots for optoelectronics. J. Mater. Chem. A **5**, 13252–13275 (2017) https://doi.org/10.1039/C7TA02076G

[2] Vasudevan, D., Gaddam, R.R., Trinchi, A., Cole, I.: Core–shell quantum dots: properties and applications. J. Alloys Compd. **636**, 395–404 (2015) https://doi.org/10.1016/j.jallcom.2015.02.102

[3] Bera, D., Qian, L., Tseng, T.K., Holloway, P.H.: Quantum dots and their multimodal applications: a review. Materials **3**, 2260–2345 (2010) https://doi.org/10.3390/ma3042260

[4] Dabbousi, B.O., Rodriguez-Viejo, J., Mikulec, F.V., Heine, J.R., Mattoussi, H., Ober, R., Jensen, K.F., Bawendi, M.G.: (CdSe)ZnS core-shell quantum dots: synthesis and characterization of a size series of highly luminescent nanocrystallites. J. Phys. Chem. B **101**, 9463–9475 (1997) https://doi.org/10.1021/jp971091y

[5] Hines, M.A., Guyot-Sionnest, P.: Synthesis and characterization of strongly luminescing ZnS-capped CdSe nanocrystals. J. Phys. Chem. **100**, 468–471 (1996) https://doi.org/10.1021/jp9530562

[6] Pietryga, J.M., Park, Y.-S., Lim, J., Fidler, A.F., Bae, W.K., Brovelli, S., Klimov, V.I.: Spectroscopic and device aspects of nanocrystal quantum dots. Chem. Rev. **116**, 10513–10622 (2016) https://doi.org/10.1021/acs.chemrev.6b00169

[7] Yun, J.M., Park, M.H., Kim, Y.B., Choi, M.J., Kim, S., Yi, Y., Kang, S.J.: Improvement of the stability of quantum-dot light emitting diodes using inorganic HfO_x hole transport layer. Materials **17**, 4739 (2024) https://doi.org/10.3390/ma17194739

[8] Das, S., Lenka, T.R., Talukdar, F.A., Velpula, R.T., Nguyen, H.P.T.: Design and analysis of novel high-performance III-nitride MQW-based nanowire white-LED using HfO_2/SiO_2 encapsulation. Opt. Quantum Electron. **55**, 67 (2023) https://doi.org/10.1007/s11082-022-04282-z

[9] Chern, M., Kays, J.C., Bhuckory, S., Dennis, A.M.: Sensing with photoluminescent semiconductor quantum dots. Methods Appl. Fluoresc. **7**, 012005 (2019) https://doi.org/10.1088/2050-6120/aaf6f8

[10] Torchynska, T.V., Espinola, J.C., Cano, A.D., Douda, J., Gazarian, K.: Emission of CdSe/ZnS and CdSeTe/ZnS quantum dots conjugated to IgG antibodies. Physica E **51**, 60–64 (2013) https://doi.org/10.1016/j.physe.2012.11.025

[11] Chang, K.P., Wu, C.J., Lo, C.W., Lin, Y.S., Yen, C.C., Wuu, D.S.: Synthesis of SiO_2-coated CdSe/ZnS quantum dots using various dispersants in the photoresist for color-conversion micro-LED displays. Mater. Sci. Semicond. Process. **148**, 106790 (2022) https://doi.org/10.1016/j.mssp.2022.106790

[12] Dortaj, H., Faraji, M., Matloub, S.: High-speed and high-contrast two-channel all-optical modulator based on solution-processed CdSe/ZnS quantum dots. Sci. Rep. **12**, 12778 (2022) https://doi.org/10.1038/s41598-022-17162-1

[13] Kapoor, S., Rodek, A., Mikołajczyk, M., Szuniewicz, J., Sośnicki, F., Kazimierczuk, T., Karpiński, M.: Electro-optic frequency shift of single photons from a quantum dot. Nanophotonics **14**, 1775–1782 (2025) https://doi.org/10.1515/nanoph-2024-0677

[14] Mantashian, G.A., Mantashyan, P.A., Hayrapetyan, D.B.: Modeling of quantum dots with the finite element method. Computation **11**, 5 (2023) https://doi.org/10.3390/computation11010005

[15] Heyn, C., Radu, A., Vinasco, J.A., Laroze, D., Restrepo, R.L., Tulupenko, V., Duque, C.A.: Exciton states in conical quantum dots under applied electric and magnetic fields. Opt. Laser Technol. **139**, 106953 (2021) https://doi.org/10.1016/j.optlastec.2021.106953

[16] Naifar, A., Hasanirokh, K.: Tuning of nonlinear optical properties by size, surrounding oxides and photonic intensity in CdSe/ZnS cylindrical core/shell quantum dot-oxide pattern and its inverted configurations. Appl. Phys. A **131**, 990 (2025) https://doi.org/10.1007/s00339-025-09128-z

[17] Zeiri, N., Naifar, A., Ben Nasrallah, S.A., Said, M.: Impact of dielectric environment on the linear and nonlinear optical properties for CdS/ZnS cylindrical core/shell quantum dots. Chem. Phys. Lett. **744**, 137215 (2020) https://doi.org/10.1016/j.cplett.2020.137215

[18] Hasanirokh, K., Naifar, A.: Inspecting the impact of decisive factors on the

second- and third-harmonic generation in cylindrical core/shell/shell quantum dot (CCSSQD) with hydrogenic impurity. Eur. Phys. J. Plus **138**, 1–16 (2023) https://doi.org/10.1140/epjp/s13360-023-04610-4

[19] Melono, R.M., Abdoulaï, A.N., Motapon, O.: Assessing magnetization and magnetic susceptibility of inverted core/shell spherical one-electron quantum dots: size and off-center displacement effects. Eur. Phys. J. Plus **139**, 948 (2024) https://doi.org/10.1140/epjp/s13360-024-05725-y

[20] Jang, Y., Shapiro, A., Isarov, M., Rubin-Brusilovski, A., Safran, A., Budniak, A.K., Lifshitz, E.: Interface control of electronic and optical properties in IV–VI and II–VI core/shell colloidal quantum dots: a review. Chem. Commun. **53**, 1002–1024 (2017) https://doi.org/10.1039/C6CC08742F

[21] Brus, L.E.: Electron–electron and electron-hole interactions in small semiconductor crystallites: the size dependence of the lowest excited electronic state. J. Chem. Phys. **80**, 4403–4409 (1984) https://doi.org/10.1063/1.447218

[22] Norris, D.J., Bawendi, M.G.: Measurement and assignment of the size-dependent optical spectrum in CdSe quantum dots. Phys. Rev. B **53**, 16338–16346 (1996) https://doi.org/10.1103/PhysRevB.53.16338

[23] Ekimov, A.I., Hache, F., Schönnauer, M.C., Ricard, D., Flytzanis, C., Kudryavtsev, I.A., Yazeva, T.V., Rodina, A.V., Efros, A.L.: Absorption and intensity-dependent photoluminescence measurements on CdSe quantum dots: assignment of the first electronic transitions. J. Opt. Soc. Am. B **10**, 100–107 (1993) https://doi.org/10.1364/JOSAB.10.000100

[24] Ibnaouf, K.H., Prasad, S., Al Salhi, M.S., Hamdan, A., Zaman, M.B., Mir, L.E.: Influence of the solvent environments on the spectral features of CdSe quantum dots with and without ZnS shell. J. Lumin. **149**, 369–373 (2014) https://doi.org/10.1016/j.jlumin.2014.01.059

[25] Jung, J.Y., Shim, Y.S., Kim, Y.K.: Improved stability of CdSeS/ZnS quantum dots against temperature, humidity, and UV-O_3 by encapsulation in crosslinked polystyrene beads. J. Mater. Sci. **56**, 12315–12325 (2021) https://doi.org/10.1007/s10853-021-06028-6

[26] Golovan, L.A., Elopov, A.V., Zaitsev, V.B., Ezhov, A.A., Zhigunov, D.M., Karpov, O.N., Talroze, R.V.: Photoluminescence of CdSe and CdSe/ZnS quantum dots in amorphous and liquid-crystalline polymer matrices. Polym. Sci. Ser. A **62**, 701–713 (2020) https://doi.org/10.1134/S0965545X20060036

[27] Lambora, S., Bhardwaj, A.: Role of dielectric medium on optical behaviour of blue emitting colloidal MoS_2 quantum dots. J. Lumin. **255**, 119598 (2023) https://doi.org/10.1016/j.jlumin.2022.119598

[28] Palade, C., Slav, A., Cojocaru, O., Teodorescu, V.S., Stoica, T., Ciurea, M.L., Lepadatu, A.M.: SiGeSn quantum dots in HfO_2 for floating gate memory capacitors. Coatings **12**, 348 (2022) https://doi.org/10.3390/coatings12030348

[29] Zeng, Z., Paspalakis, E., Garoufalis, C.S., Terzis, A.F., Baskoutas, S.: Optical susceptibilities in singly charged ZnO colloidal quantum dots embedded in different dielectric matrices. J. Appl. Phys. **113**, 054303 (2013) https://doi.org/10.1063/1.4789363

[30] Elamathi, M., Peter, A.J., Lee, C.W.: Role of various dielectric environment matrices of InP/ZnS core/shell quantum dot on optical gain coefficient. Eur. Phys. J. D **74**, 1–8 (2020) https://doi.org/10.1140/epjd/e2020-10094-3

[31] Yahayaoui, N., Zeiri, N., Baser, P., Said, M., Saadaoui, S.: Influence of the size and dielectric environments on the optical properties in CdS/ZnS core–shell quantum dot. Plasmonics **18**, 1489–1498 (2023) https://doi.org/10.1007/s11468-023-01862-3

[32] Amin, N., Peter, A.J.: Role of surrounding dielectric matrices on the nonlinear properties of group II–VI core/shell dot in the presence of electric field. Micro Nanostruct. **185**, 207728 (2023) https://doi.org/10.1016/j.micrna.2023.207728

[33] Anchala, A., Purohit, S.P., Mathur, K.C.: Third harmonic generation in intraband transitions of spherical silicon quantum dots. J. Appl. Phys. **112**, 094306 (2012) https://doi.org/10.1063/1.4764347

[34] Robertson, J.: High dielectric constant oxides. Eur. Phys. J. Appl. Phys. **28**, 265–291 (2004) https://doi.org/10.1051/epjap:2004206

[35] Wang, K., Lu, J., Xiang, Z., Wang, Z., Jin, H., Li, R., Jiang, R.: Engineering improvement of the core layers of charge trapping flash memory based on doped HfO_2 and segmented fabrication. Electronics **13**, 1642 (2024) https://doi.org/10.3390/electronics13091642

[36] Seckin, A., Koralay, H.: Electrical properties of Schottky devices from HfO_2 and ZnO/HfO_2 thin films: morphological, structural, and optical investigations. ACS Omega **10**, 6520–6533 (2025) https://doi.org/10.1021/acsomega.4c08878

[37] Hemdana, I., Mahdouani, M., Bourguiga, R.: Investigation of the third-order nonlinear optical susceptibilities associated with intersubband transitions in $CdSe/ZnS/SiO_2$ core/shell/shell quantum dot. Superlattices Microstruct. **60**, 336–348 (2013) https://doi.org/10.1016/j.spmi.2013.05.019

[38] Jaouane, M., Sali, A., Kasapoglu, E., Ungan, F.: Tuning of nonlinear optical characteristics of a cylindrical quantum dot by external fields and structure parameters. Philos. Mag. **103**, 693–711 (2023) https://doi.org/10.1080/14786435.2023.2165194

[39] Hbibi, M., Mommadi, O., Chouef, S., Boussetta, R., Belamkadem, L., El Moussaouy, A., Duque, C.A.: Finite confinement potentials, core and shell size effects on excitonic and electron-atom properties in cylindrical core/shell/shell quantum dots. Sci. Rep. **12**, 14854 (2022) https://doi.org/10.1038/s41598-022-19118-3

[40] Mommadi, O., Hbibi, M., Chouef, S., Boussetta, R., Chnafi, M., El Moussaouy, A., Duque, C.A.: Behavior of optoelectronic properties of exciton–phonon in a multilayered cylindrical quantum well wires-dot with two finite confinement potentials structures. Mater. Sci. Semicond. Process. **168**, 107805 (2023) https://doi.org/10.1016/j.mssp.2023.107805

[41] Kumagai, M., Takagahara, T.: Excitonic and nonlinear-optical properties of dielectric quantum-well structures. Phys. Rev. B **40**, 12359–12381 (1989) https://doi.org/10.1103/PhysRevB.40.12359

[42] Bolcatto, P.G., Proetto, C.R.: Partially confined excitons in semiconductor nanocrystals with a finite size dielectric interface. J. Phys.: Condens. Matter **13**, 319–334 (2001) https://doi.org/10.1088/0953-8984/13/2/309

[43] Rudin, S., Reinecke, T.L., Segall, B.: Temperature-dependent exciton linewidths in semiconductors. Phys. Rev. B **42**, 11218–11231 (1990) https://doi.org/10.1103/PhysRevB.42.11218

[44] Empedocles, S., Bawendi, M.: Spectroscopy of single CdSe nanocrystallites. Acc. Chem. Res. **32**, 389–396 (1999) https://doi.org/10.1021/ar9501939

[45] Alam, S., Paul, P., Beladiya, V., Schmitt, P., Stenzel, O., Trost, M., Szeghalmi, A.: Heterostructure films of SiO_2 and HfO_2 for high-power laser optics prepared by plasma-enhanced atomic layer deposition. Coatings **13**, 278 (2023) https://doi.org/10.3390/coatings13020278

[46] Vurgaftman, I., Meyer, J.R., Ram-Mohan, L.R.: Band parameters for III–V compound semiconductors and their alloys. J. Appl. Phys. **89**, 5815–5875 (2001) https://doi.org/10.1063/1.1368156

[47] Adachi, S.: Properties of Group-IV, III–V and II–VI Semiconductors. Wiley, Chichester (2005)

[48] Efros, A.L., Rosen, M.: The electronic structure of semiconductor nanocrystals. Annu. Rev. Mater. Sci. **30**, 475–521 (2000) https://doi.org/10.1146/annurev.matsci.30.1.475

[49] Madelung, O.: Semiconductors: Data Handbook, 3rd edn. Springer, Berlin (2004)

[50] BenDaniel, D.J., Duke, C.B.: Space-charge effects on electron tunneling. Phys. Rev. **152**, 683–692 (1966) https://doi.org/10.1103/PhysRev.152.683

[51] Bastard, G.: Wave Mechanics Applied to Semiconductor Heterostructures. Les Editions de Physique, Paris (1988)

[52] Kala, A., Achanta, V.G.: Dielectric encapsulations suitable for applications in quantum technologies. Eur. Phys. J. Spec. Top. **231**, 799–805 (2022) https://doi.org/10.1140/epjs/s11734-021-00388-3

[53] Brus, L.E.: A simple model for the ionization potential, electron affinity, and aqueous redox potentials of small semiconductor crystallites. J. Chem. Phys. **79**, 5566–5571 (1983) https://doi.org/10.1063/1.445676

[54] Franceschetti, A., Williamson, A., Zunger, A.: Addition spectra of quantum dots: the role of dielectric mismatch. J. Phys. Chem. B **104**, 3398–3401 (2000) https://doi.org/10.1021/jp993721v

[55] Efros, A.L., Efros, A.L.: Interband absorption of light in a semiconductor sphere. Sov. Phys. Semicond. **16**, 772–775 (1982)

[56] Kayanuma, Y.: Quantum-size effects of interacting electrons and holes in semiconductor microcrystals with spherical shape. Phys. Rev. B **38**, 9797–9805 (1988) https://doi.org/10.1103/PhysRevB.38.9797

[57] Takagahara, T.: Effects of dielectric confinement and electron-hole exchange interaction on excitonic states in semiconductor quantum dots. Phys. Rev. B **47**, 4569–4584 (1993) https://doi.org/10.1103/PhysRevB.47.4569

[58] Laheld, U.E.H., Einevoll, G.T.: Excitons in CdSe quantum dots. Phys. Rev. B **55**, 5184–5204 (1997) https://doi.org/10.1103/PhysRevB.55.5184

[59] Murray, C.B., Norris, D.J., Bawendi, M.G.: Synthesis and characterization of nearly monodisperse CdE (E = S, Se, Te) semiconductor nanocrystallites. J. Am. Chem. Soc. **115**, 8706–8715 (1993) https://doi.org/10.1021/ja00072a025

[60] Talbi, A., El Haouari, M., Nouneh, K., Pérez, L.M., Tiutiunnyk, A., Laroze, D., Feddi, E.: LO-phonons and dielectric polarization effects on the electronic properties of doped GaN/InN spherical core/shell quantum dots in a non-parabolic band model. Appl. Phys. A **127**, 1–17 (2021) https://doi.org/10.1007/s00339-021-04489-7

[61] Jain, P.K., Ghosh, D., Baer, R., Rabani, E., Alivisatos, A.P.: Near-field manipulation of spectroscopic selection rules on the nanoscale. Proc. Natl. Acad. Sci. USA **109**, 8016–8019 (2012) https://doi.org/10.1073/pnas.1120984109

[62] Boyd, R.W.: Nonlinear Optics, 3rd edn. Academic Press, Amsterdam (2008)

[63] Haug, H., Koch, S.W.: Quantum Theory of the Optical and Electronic Properties of Semiconductors, 5th edn. World Scientific, Singapore (2009)

[64] Mukamel, S.: Principles of Nonlinear Optical Spectroscopy. Oxford University Press, New York (1995)

[65] Ahn, D., Chuang, S.L.: Calculation of linear and nonlinear intersubband optical absorptions in a quantum well model with an applied electric field. IEEE J. Quantum Electron. **23**, 2196–2204 (1987) https://doi.org/10.1109/JQE.1987.1073301

[66] Guo, A., Bhattacharya, P., Yuan, P., Ghosh, A.: Nonlinear optical properties of quantum-dot structures. Phys. Rev. B **47**, 10307–10315 (1993) https://doi.org/10.1103/PhysRevB.47.10307